Waste Management 177 (2024) 56–65

Contents lists available at ScienceDirect

Waste Management

journal homepage: www.elsevier.com/locate/wasman

Research Paper

Morphology and phosphate distribution in bottom ash particles from fixed-bed co-combustion of sewage sludge and two agricultural residues

Anna Strandberg [a,b,*], Mikael Thyrel [b], Joel Falk [c], Marcus Öhman [c], Nils Skoglund [a]

[a] Umeå University, Department of Applied Physics and Electronics, Thermochemical Energy Conversion Laboratory, SE 901 87 Umeå, Sweden
[b] Swedish University of Agricultural Sciences, Department of Forest Biomaterials and Technology, SE 901 83 Umeå, Sweden
[c] Energy Engineering, Department of Engineering Sciences and Mathematics, Luleå University of Technology, SE-97187 Luleå, Sweden

A B S T R A C T

The purpose of this study was to provide detailed knowledge of the morphological properties of ash particles, including the volumetric fractions and 3D distributions of phosphates that lay within them. The ash particles came from digested sewage sludge co-combusted with K- and Si-rich wheat straw or K-rich sunflower husks. X-ray micro-tomography were combined with elemental composition and crystalline phase information to analyse the ash particles in 3D.

Analyses of differences in the X-ray attenuation enabled calculation of 3D phosphate distributions that showed high heterogeneity in the slag particles. This is underscored by a distinct absence of phosphates in iron-rich and silicon-rich parts. The slag from silicate-based wheat straw mixtures had lower average attenuation than that from sunflower husks mixtures, which contained more calcium. Calculated shares of phosphates between 7 and 17 vol% were obtained, where the highest value for a single assigned phosphate was observed in hard slag from wheat straw with 10 % sewage sludge. The porosity was notably higher for particles from pure wheat straw combustion (62 vol%), compared to the other samples (15–35 vol%). A high open pore volume fraction (60–97 vol%) indicates that a large part of the pores can be accessed by the surroundings. For all samples, more than 60 % of the discrete (closed) pores had an equivalent diameter < 30 μm, while the largest volume fraction consisted of pores with an equivalent diameter > 75 μm. Slag from sunflower husk mixtures had larger pore volumes and a greater relative number of discrete pores >75 μm compared to wheat straw mixtures.

1. Introduction

Phosphorus (P) is an essential nutrient, and its availability and distribution in soil profiles influence plant growth. The P cycle was identified as one of the planetary boundaries that we must remain within to avoid major human-induced environmental changes at a global level (Richardson et al., 2023; Rockström et al., 2009; Steffen et al., 2015). The raw material for the production of mineral fertiliser is phosphate rock, which is a limited resource. Phosphate rock reserves are geographically concentrated in Morocco and Western Sahara that hold >70 % of the presently known global P-rock reserves. With continuing global consumption, the shares of these countries will likely increase in the future (Cooper et al., 2011; Zhu et al., 2023). The P flows and balances of the European Union Member States were analysed by Van Dijk et al. (2016), revealing a generally large dependency on P-rock import and long-term accumulation in agricultural soils while large P losses occurred due to relatively low recycling and low-efficiency use. It is important to increase P recycling in society in an effective and sustainable way.

The major P waste flow in Europe is domestic wastewater, of which municipal sewage sludge makes up the largest part (Schoumans et al., 2015; Van Dijk et al., 2016). Using sewage sludge in high temperature combustion systems is one way to support heat and power production while recycling macro- and micro-nutrients as well as destroying organic contaminants and pathogens at the same time (Krüger and Adam, 2015). With the aim to make P in the ash more plant-available, sewage sludge can be co-combusted with some other residual biomass (Falk et al., 2023; Häggström et al., 2021; Hannl et al., 2020; Lidman Olsson et al., 2023; Zhao et al., 2018). For example, wheat straw is an agricultural residue, usually quite rich in potassium (K), that has been shown to promote the formation of mixed cation phosphates that increase plant availability compared to sewage sludge ash alone (Herzel et al., 2021; Herzel et al., 2016).

Ash residues containing trace elements such as arsenic (As), mercury (Hg) and cadmium (Cd) can be formed during combustion. However, a separation between nutrients and potentially toxic trace elements can be achieved at higher temperatures, where most trace elements are volatilised (Moller et al., 2007; Nordin et al., 2020; Van de Velden et al., 2008). P has been shown to remain in coarse ash fractions to a large extent, such as the bed/bottom ash fractions from fluidized bed or grate-

* Corresponding author at: Umeå University, Department of Applied Physics and Electronics, Thermochemical Energy Conversion Laboratory, SE 901 87 Umeå, Sweden.
E-mail address: anna.strandberg@umu.se (A. Strandberg).

https://doi.org/10.1016/j.wasman.2024.01.040
Received 25 September 2023; Received in revised form 15 January 2024; Accepted 23 January 2024
Available online 29 January 2024

fired conversion, which can then be used for recycling (Falk et al., 2020a; Falk et al., 2020b; Hedayati et al., 2022; Pettersson et al., 2008; Skoglund et al., 2014).

The strategies available for recycling involve either post-treatment – with approaches such as acidic digestion or leaching and thermochemical treatment (Kratz et al., 2019; Zhu et al., 2023) – or direct use as fertilisers under the new EU regulation by the European Parliament and Council (2023). If it is possible to form phosphates suitable for direct ash recovery from the thermal process, they should have properties that motivate their use, such as a relatively low Ca/P ratio compared to P-containing ores.

Attaining effective and sustainable nutrient return requires a thorough understanding of the distribution of P and the phosphates that are formed, including their relationship to the physical properties of ash particles. This could be of importance to judge if post-treatment (e.g. milling the ashes) is required for the plant roots to access the nutrients. Studies on how ash particles affect the soil are rare, although experiences from biochars can serve as an interesting comparison. Porosity, including pore volume and size distribution, is important for the leaching and water holding capacity of biomass chars (Edeh et al., 2020; Rasa et al., 2018). The ability of the soil to transmit and store water depends on the pore size distribution. Within soil aggregates, larger pores defined as having diameters over 30 μm are generally filled with air can transmit water whereas smaller pores can store water (Cameron and Buchan, 2017).

Previous research has shown that co-combustion of digested sewage sludge with K- and Si-rich wheat straw or K-rich sunflower husks produces ashes rich in nutrients such as P, K and Ca (Falk et al., 2023). These ashes have the potential to be used directly for fertilisation due to their porosities and open pore volumes that enable an exchange of P via pore water or direct biological interaction. Their thin particle walls may also lead to rapid weathering that further enhance the potential for significant interaction and nutrient transport with soil water (Strandberg et al., 2021). Knowledge of the distribution of the nutrients in the ash particle would be valuable complementing information to develop strategies for efficient and sustainable nutrient recycling. Previous studies on the distribution of P and other elements in ash particles have usually been performed by elemental mapping with, e.g. scanning electron microscopy with energy dispersive X-ray spectroscopy (SEM-EDS) (Falk et al., 2023; Hedayati et al., 2022; Reinmöller et al., 2019). However, those studies were limited to the analysis of one or a few cross-sections of samples that provided compositional data at a depth of approximately 3–5 μm from the surface. In this study, we employed the more comprehensive method X-ray micro-tomography (XRT), a non-destructive technique that reveals the internal structure of objects in 3D via variations in density and elemental composition. Different materials can be distinguished, segmented, and quantified in an object based on differences in the X-ray attenuation (Kalasová et al., 2018; Mees et al., 2003; Strandberg et al., 2018).

Ash particles from fixed-bed co-combustion of digested sewage with K- and Si-rich wheat straw or K-rich sunflower husks were obtained. The objective of this study was to provide detailed knowledge about these ash particles concerning their morphological properties as well as the volumetric share and 3D distribution of phosphates that lay within them. This was achieved by a combination of X-ray based techniques, where 3D models obtained by XRT were interpreted with support from elemental analysis using SEM-EDS and crystalline compounds identified by X-ray diffraction (XRD). Using this novel approach for the analysis of the ash particles, a calculated phosphate distribution in 3D was obtained by associating the intensity of the X-ray attenuation of each voxel to chemical composition. Additionally, the samples were evaluated according to morphology, porosity, open pore volume, pore size distribution and sphericity.

2. Material and methods

2.1. Material

Slag particles (sintered ash) from fixed-bed combustion in an under-fed pellet burner with mixtures of digested sewage sludge (SS), wheat straw (WS) and sunflower husks (SH) have been examined in 3D to reveal their morphological properties and compositional distributions. The fuel properties, combustion experiment and ash characterisation have previously been described by Falk et al. (2023). The slag particles come from combustion experiments with different pelleted fuel mixtures (on a dry basis): 100 wt% wheat straw (WS), 90 wt% wheat straw and 10 wt% sewage sludge (WSS10), 70 wt% wheat straw and 30 wt% sewage sludge (WSS30), 85 wt% sunflower husks and 15 wt% sewage sludge (SHS15), and 60 wt% sunflower husks and 40 wt% sewage sludge (SHS40). The purpose of the different fuel mixtures was to have one set with a higher level of agricultural residue addition (90 wt% wheat straw and 85 wt% sunflower husks) and one set with a lower addition (70 wt% wheat straw and 60 wt% sunflower husks), in order to achieve different composition of the ash forming elements; more information can be found in Falk et al. (2023). The mono-combustion of SS pellets was poor due to the high ash content. To lower the ash content, SS was mixed with softwood pellets to achieve better combustion performance without significantly changing the overall ash composition (SS ash > 97 wt% of total). Therefore, an additional analysis was performed on particles from the combustion of sewage sludge pellets mixed with softwood pellets, labelled SS33.

The under-fed burner, with a maximum nominal power output of 20 kW, was manufactured by EcoTec (Sweden) and the burner was installed in a reference boiler (Combifire, Sweden). The experiment was performed with excess air, resulting in approximately 10 vol% O_2 in the flue gas.

Sintered ash particles (so-called slag) from the bottom ash from each combustion experiment were taken for analysis. The slag particles were divided into two grades depending on size and durability: hard slag (durable pieces of slag) and weak slag (easily broken by hand). For WSS10 and WSS30, both hard slag and weak slag were analysed, while for the other fuels, only hard slag was analysed. Hard slag particles from combustion of the different mixtures are shown in Figure S1, Supplementary data.

2.2. X-ray micro-tomography and image analysis

Imaging of the slag particles with X-ray micro-tomography (XRT) was performed with a *GE Phoenix v|tome|x m* X-ray scanner located at the X-ray facility at the Department of Soil and Environment at the Swedish University of Agriculture (Uppsala, Sweden). The device has a 240 kV X-ray tube, a tungsten target and a GE 16″ flat-panel detector with 2024 × 2024 detector crystals. The scans were carried out at a voltage of 60 kV, and the electron flux was 150 μA. During a 360° rotation of the samples, 2000 radiographs were collected with regular angular intervals. The exposure time for each radiograph was 333 ms. A sample holder of aluminium, 6 cm high and with a 6.5 mm inner diameter, was used to stabilise the sample, and it was used as an optical filter to reduce beam-hardening artefacts. The images were reconstructed with the GE software datos|×, resulting in a 3D stack of images with a spatial resolution of 6.4 μm in all directions. Two replicates of each fraction were examined. These replicates were taken from different slag lumps and broken into a size that could be accommodated by the sample holder (max 6.5 mm in diameter).

The free and open image processing software packages Fiji (Fiji Is Just ImageJ) (Schindelin et al., 2012; Schneider et al., 2012) and Avizo 9.3 (Fei VSG Inc., Burlingham, MA) were used to perform image analyses and visualisation of 3D tomographic volumes.

The reconstructed images have a brightness intensity associated with each voxel that corresponds to the degree of attenuation of the X-rays.

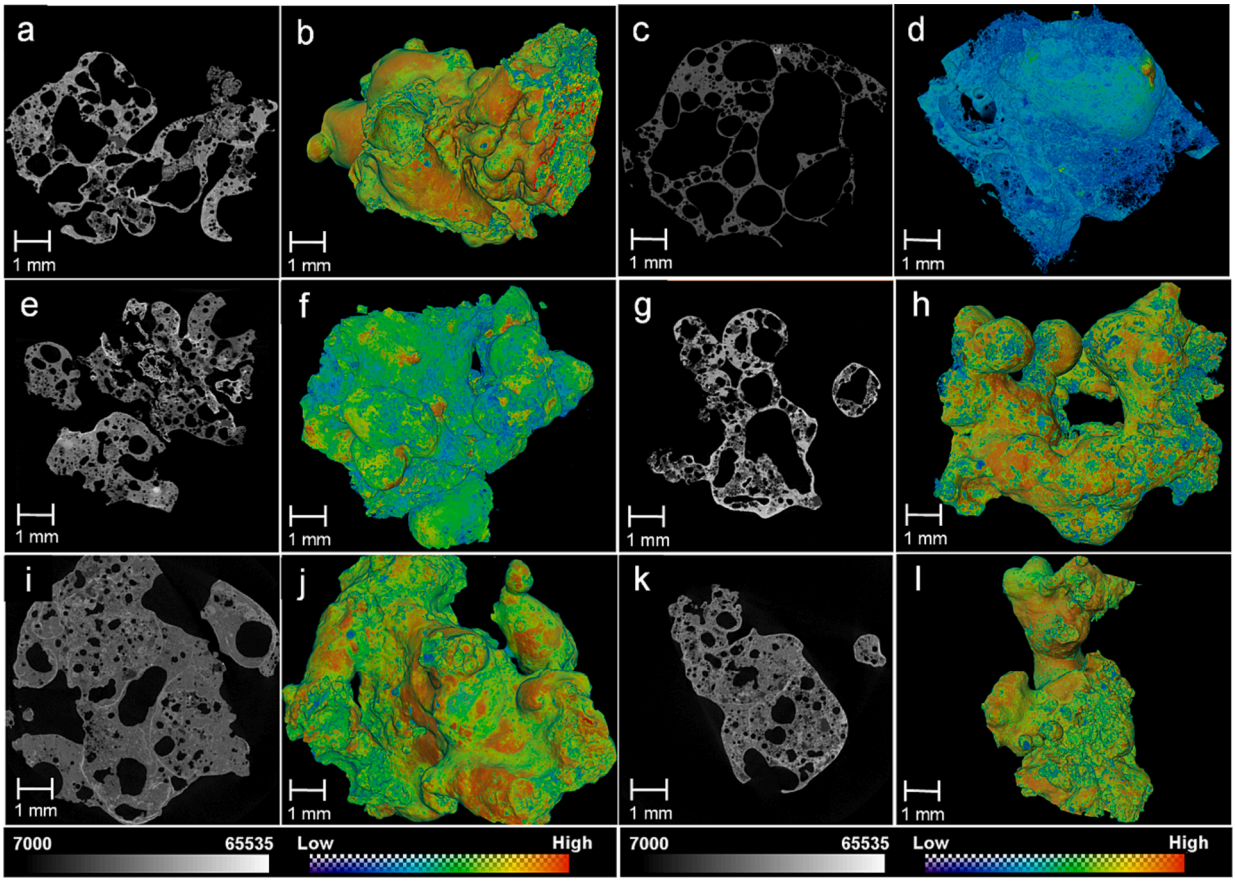

Fig. 1. Cross-sections and 3D reconstructions from data produced by XRT scanning of particles of hard slag from a-b) SS33, c-d) WS, e-f) WSS10, g-h) WSS30, i-j) SHS15, and k-l) SHS40. Gray and colour scales apply to X-ray attenuation intensities for cross-sections and 3D reconstructions, respectively.

The differences in attenuation depend on the X-ray energy and the material density and mass, as well as the proton number and electron density of the elements in the scanned sample. Moreover, the maximum intensity values obtained from the reconstructed images can differ between samples. This problem may arise for images acquired with beams from X-ray tubes, and it is explained in more detail by Koestel and Larsbo (2014). Due to abrasions on the anode material from electrons generating the X-rays, shifting brightness distributions of the emitted beam from the X-ray tube can occur over time. This leads to fluctuation of the brightness in the X-ray images. To correct for this, SoilJ (Koestel, 2018), which is a plugin for Fiji/ImageJ, was used to calibrate the brightness for the different samples to one standard scale. SoilJ uses the intensity values of two reference points. Here, the wall of the aluminium sample holder and the air were used as both have constant density. The intensity values for the original X-ray images were normalised using the reference values. The images with the standardised values were then used for further analysis in this work. The plugin can also automatically detect outlines of the wall of the sample holder and identifies the top and bottom of the sample holder. All cross-section images above and below the detected top and bottom, respectively, were removed from the 3D stack. After this, the sample holder was removed. To reduce the file size and to limit the computation time, horizontal layers on the top and bottom that were not part of the sample were also removed.

Different elements have different attenuation coefficients. Reference values of the total attenuation coefficient were obtained from XCOM: Photon Cross Sections Database, NIST Standard Reference Database 8 (Berger et al., 2010). Attenuation without/with limited coherent scattering was assumed. By using compounds that are clear and easy to identify in the samples, a linear adjustment was made for the intensity in the samples. Areas/grains with iron oxide and quartz appear clearly in the samples, and can also be recognized by shape from SEM-EDS; therefore, they have been used for this purpose. Tabulated X-ray attenuation coefficients for the crystalline phases in the sample previously identified in the samples with powder XRD (Falk et al., 2023) were used. By using linear adjustment, the intensity value for each of the crystalline phases was calculated. The volumetric share and the distribution of phosphates and other compounds were then identified based on their correspondence with the intensity values.

An extensive part of the pores was connected with the background, henceforth called open pores. The other, unconnected pores are called discrete pores. For the analysis of porosity, open pore volume, pore size distribution and sphericity, the images were processed with binary segmentation to identify slag and pores/background. The pores and background were then separated and labelled according to the process described in a previous work by Strandberg et al. (2021). The porosity is the volume fraction of the sample that consists of pores (both open and discrete pores). Pore volume and pore size were calculated, which was estimated using equivalent diameter.

The sphericity was calculated for the pores in each respective particle. Sphericity is a measure of how spherical the pores are and can be defined as

$$\varphi = \frac{\pi^{1/3}(6V)^{2/3}}{A}$$

where V is the volume and A the surface area of a pore. A sphericity that is less than one means that the pores are not spherical.

2.3. Scanning electron microscopy

The chemical composition and morphology were characterised by

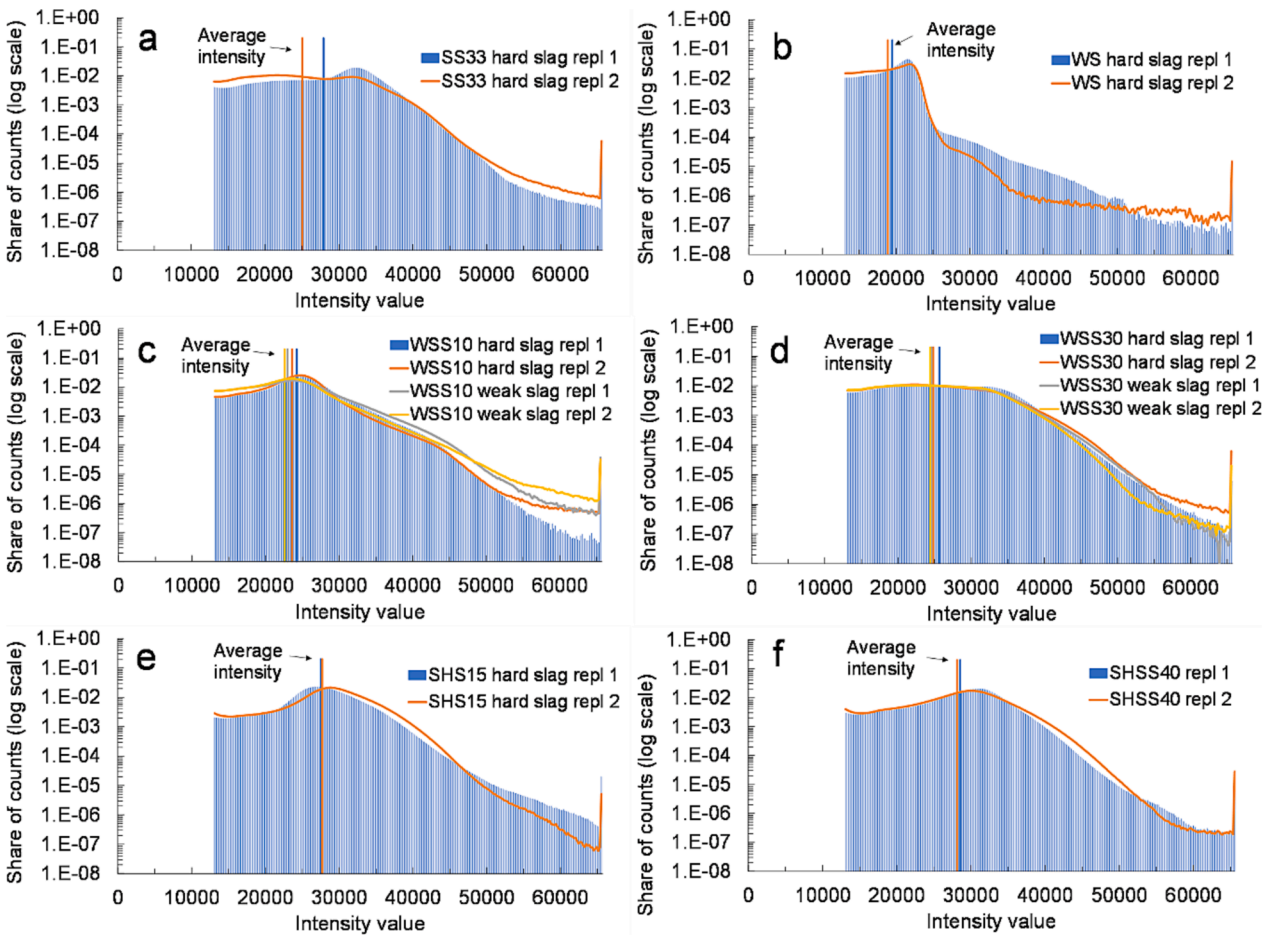

Fig. 2. Histograms showing normalised X-ray attenuation intensities, without background and pores, for a) SS33, b) WS, c) WSS10, d) WSS30, e) SHS15, and f) SHS40. Mean intensity values indicated with a line. The range of the intensity for the particles were 13107–65535.

analysis with variable-pressure scanning electron microscopy (VP-SEM; Carl Zeiss Evo LS-15). The samples were cast in epoxy, polished with silicon carbide paper to obtain a smooth cross-section, and then analysed. An acceleration voltage of 15 kV and a probe current of 400 pA were used. A backscattered electron detector was used for imaging. Elemental analysis was performed at different parts of the samples with an energy dispersive X-ray spectrometer (EDS; Oxford Instruments X-Max 80 mm^2), with a combination of point and area analyses and elemental mapping.

3. Results and discussion

3.1. Morphological properties

Co-combustion of wheat straw and digested sewage sludge gave more heterogeneous slag compared to the combustion of pure wheat straw. Fig. 1 visualises slag particles with cross-sections and corresponding 3D reconstructions. The cross-sections display X-ray attenuation intensity maps, where brighter portions have higher attenuation and are comprised of heavier ash forming elements, i.e. ash-forming elements. These include iron-rich melts or crystalline compounds, as confirmed by Falk et al. (2023). The darker portions are char residuals (the carbon matrix), and the completely black spots represent voids (air). The 3D reconstructions are colour-mapped according to attenuation, from blue (low attenuation) to red (high attenuation).

SS33 was not completely converted during the combustion process. Tomographic scanning of the particles revealed that residual char remains inside the particle to a fairly large extent, as indicated with an arrow in Figure S2, Supplementary data. Particles that have not undergone complete thermal conversion will have higher heterogeneity in X-ray attenuation, i.e. they will appear as less homogeneous particles in XRT. This may explain the greater differences in mean intensity value for SS33 compared to the other samples, as shown in Fig. 2a. Fig. 2 also shows that there is a difference in attenuation, both in the mean value of the intensity and shape of the histogram, between the different types of fuel ashes. The silicate-based wheat straw slag (Fig. 2b) has the lowest attenuation values, followed by the lowest blend of WS and SS (Fig. 2c). SS33 is similar in shape to mixtures with a high share of sewage sludge (Fig. 2a, d, and f), indicating that sewage sludge ash dominates overall ash composition heavily at this admixing level. The sunflower husks mixtures are similar in average intensity values (Fig. 2e and f) but differ in the shape of the curves. The mixtures with wheat straw display slightly lower values compared to the more Ca-dominated sunflower husks. There is no noticeable difference between hard slag and weak slag for the WSS10 and WSS30 samples.

3.2. Phosphate distribution

A backscatter detector was used for imaging with SEM-EDS. Fig. 3 shows an example of a P-rich region in a weak slag ash particle from the combustion of WSS10. Overall, elemental maps show that Si is found almost over the entire sample, mostly associated with K and Al. Si was also found as discrete particles, probably originating from the sewage sludge. To a large extent, P is found together with Ca. The chart of the relative compositions for the numbered spots shows that there are also small areas with high amounts of P together with other elements, e.g. K,

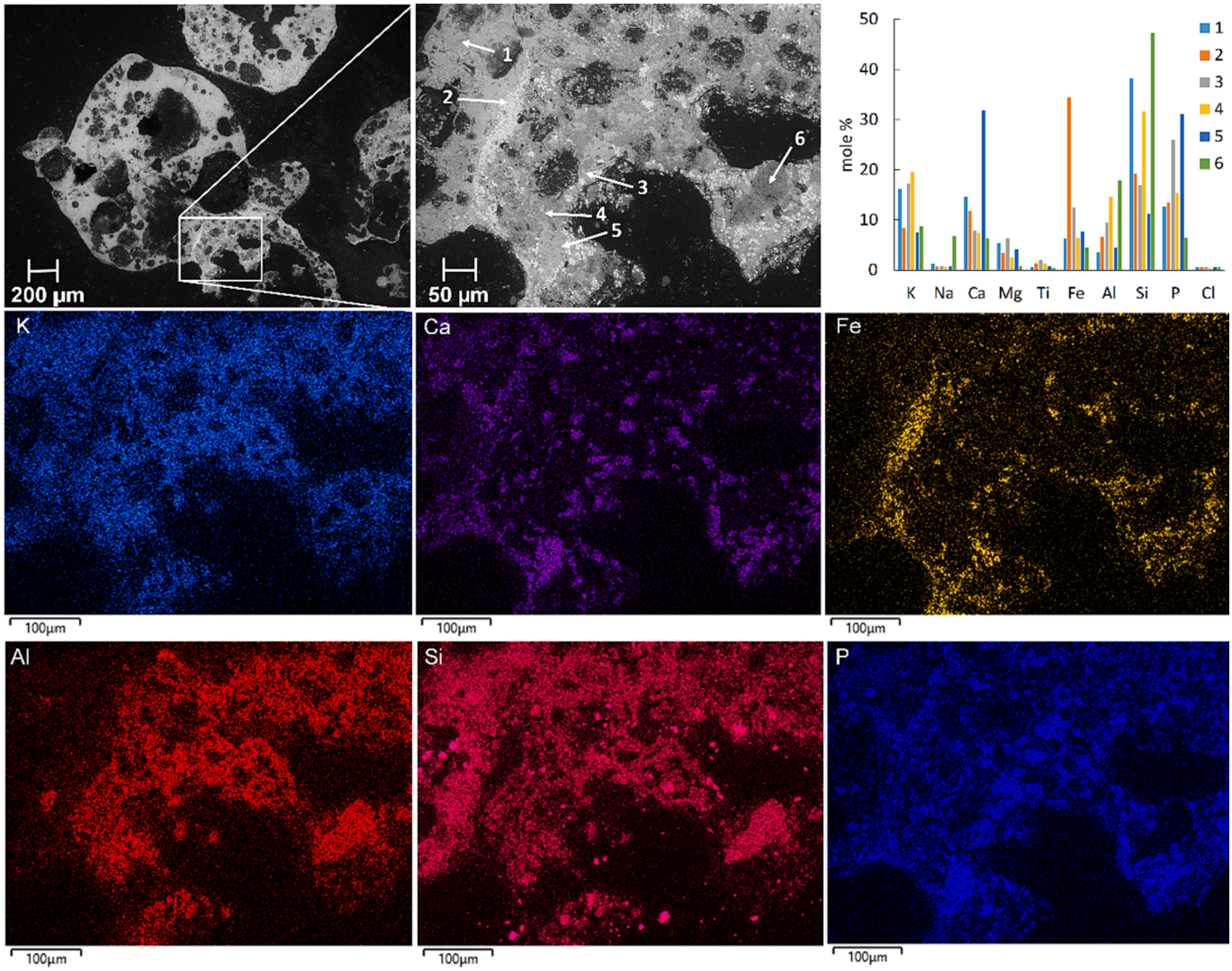

Fig. 3. SEM backscatter electron image of a P-rich part of the WSS10 weak slag, showing morphology, relative compositions at numbered spots on a C- and O-free basis, and elemental maps of the enlarged view that show the distributions of K, Ca, Fe, Al, Si and P.

Si, Fe (no.3).

Analyses of differences in the X-ray attenuation enabled the 3D distribution and volumetric share of phosphates in the slag particles to be calculated. X-ray attenuation coefficients (Berger et al., 2010) were used to make a linear adjustment to the intensities in the samples. In Fig. S3a, Supplementary data, areas/grains with iron oxide and quartz compounds in the samples that are clear and easy to identify both with XRT and SEM-EDS are exemplified. Fig. S3b, Supplementary data, show the total attenuation for SiO_2 and Fe_2O_3 versus the max and min intensity values for the respective compounds from the tomographic data. The results from the linear adjustment of these data were $y_{max} = 84215x\text{-}4464.5$ and $y_{min} = 84215x\text{-}5920.5$, respectively. Calculated intensity values for the crystalline phases containing P and K, previously identified in these materials by Falk et al. (2023), can be found in Table S1, Supplementary data. The estimated volume fraction of these crystalline phases occupying the slags, based on the fraction of voxels with these intensity values, are shown in Table 1. For the WSS30 and SHS15 samples, two phosphates with overlapping values were found. Those were combined together in the evaluation. Overall, the difference between the replicates is small. WSS30 has a comparable volume fraction of the crystalline phases for the hard slag and the weak slag particles, while for WSS10, the hard slag particles have a higher fraction of the phosphates and a lower fraction of potassium aluminium silicate.

The volume fraction of the crystalline phases is, however, difficult to directly compare with the quantification of crystalline phases from XRD, as presented by Falk et al. (2023) (given in weight percent). Data from Falk et al. (2023) show that the bulk amorphous share of the samples varied between 36 wt% and 63 wt% (SHS15 < SS33 < SHS40 < WSS30 < WSS10). The share of amorphous or unidentified P in that study was lower than the bulk, with 25 wt% for SS33, 35 wt% for SHS15, 40 wt% for WSS30 and SHS40, 45 wt% for WSS10. Pure wheat straw contains low levels of P, high amorphous share (93 wt%), and previous studies have shown that crystalline phases with P are rarely identified with XRD (Hedayati et al., 2022; Hedayati et al., 2021). Therefore, WS is not included in the analysis regarding phosphate distribution.

Fig. 4 shows cross-sections from the interior of hard slag particles and calculated phosphate and potassium aluminium silicate distributions for the samples. In Fig. 5, a closer view of a cross-section from the WSS10 hard slag is shown. The slag particles display high heterogeneity, but well-defined P-rich areas are evenly distributed inside the particles, likely due to local crystallisation (Fig. 4 and Fig. 5). The phosphates are distributed over most of the samples in a similar way, and there is no difference when viewing the distribution in 3D. The phosphates are separated from the iron-rich, bright parts, as well as the dark silicon-rich ones, e.g. SiO_2 and $K(AlSi_2O_6)$. This in agreement with the SEM-EDS results that show P and Ca concentrated together while P is negatively

Table 1
Volume fraction (vol%) of P- and K-containing crystalline phases found in the samples. Crystalline phases identified by Falk et al.(2023).

	Volume fraction of total voxels			
	Hard slag repl1	Hard slag repl2	Weak slag repl1	Weak slag repl2
SS33	vol%	vol%	vol%	vol%
$Ca_4(Mg, Fe)_5(PO_4)_6$	5	5	–	–
$Ca_9Al(PO_4)_7$	5	5	–	–
WSS10				
$Ca_{9.5}Mg_{0.78}Fe_{0.22}(PO_4)_7$	17	17	11	12
$KAlSi_2O_6$	4	5	7	7
WSS30				
$Ca_4(Mg,Fe)_5(PO_4)_6$ and $Ca_9Fe(PO_4)_7$	7	7	7	7
$KAlSi_2O_6$	6	6	7	7
SHS15				
$Ca_9KMg(PO_4)_7$ and $Ca_{9.5}Mg_{0.8}Fe_{0.2}(PO_4)_7$	11	8	–	–
$KAlSi_2O_6$	2	2	–	–
$KAlSiO_4$	2	2	–	–
SHS40				
$Ca_4(Mg, Fe)_5(PO_4)_6$	9	9	–	–
$Ca_9Al(PO_4)_7$	4	5	–	–
$KAlSi_2O_6$	2	3	–	–

correlated with K, Al and especially Si. The sewage sludge is rich in iron, which is used as the precipitant in the wastewater treatment plant. Fe is mainly concentrated on smaller spots or accumulated in streaks, often close to the surfaces or pores of the particles. This agrees with other studies that have shown that during combustion, iron phosphate present in sewage sludge forms insoluble iron compounds such as haematite as well as acid-soluble phosphate compounds, with their tendency for formation increasing with combustion temperature (Atienza–Martínez et al., 2014; Gorazda et al., 2012; Häggström et al., 2021).

For WSS10 and WSS30, no difference in distribution is noticeable between hard slag and weak slag particles. Cross-sections showing the distribution of P- and K-containing crystalline phases can be found in Supplementary data, Figure S4.

3.3. Pore size distribution and sphericity

The average porosity was notably higher for the pure WS sample (62 vol%) compared to the other slag fractions, while SHS15 had a significantly lower porosity (Fig. 6). The open pore volume indicates the fraction of pore volume that consists of open pores. There are similar trends between the samples in terms of their porosity and open pore volume. For the slag particles from WS and WS mixtures, a more detailed description of the microstructure are presented in Strandberg et al. (2021).

The pore size distribution (Fig. 7) shows that all slag particles have a large number of small discrete pores (lines, left axes) with a pore equivalent diameter under 30 μm, while the largest volume fraction (bars, right axes) consists of larger pores (>75 μm). This can be of importance for soil water access; small pores generally store water while pores with a minimum equivalent diameter over 30 μm transmit water (Cameron and Buchan, 2017). It is possible to see some differences between slags from different fuels. The SH-containing fuels produce slags with slightly lower relative numbers of small pores and relatively more pore volumes consisting of pores over 75 μm compared to the slags from WS-containing fuels.

The calculated sphericity of the discrete pores is shown in Figure S5, Supplementary data. The sphericity decreases with the pore equivalent diameter and, for the WS mixtures, also with the share of WS (WS > WSS10 > WSS30). On average, the WSS30 samples seem to have a lower degree of sphericity than the others, while pure wheat straw samples have a higher degree of sphericity. This could have been caused by differences in the amount of K/Ca-silicate-dominated melts—which can have a wide range of viscosities (Ma et al., 2021)—that were present in the samples. On average, pores with an equivalent diameter between the size range of 20–40 μm are not spherical. For the smallest pores, the calculated sphericity has a large uncertainty; in particular, the pores that have 1.6 as their sphericity value. A sphericity that is less than one means that the pores are not spherical.

3.4. Practical implications and outlook

Selecting an appropriate strategy to recover phosphorus from ash and slag particles is facilitated by understanding their inner morphology and phosphate distribution as a complement to conventional information about their elemental and crystalline composition. The location of phosphorus within slag and ash particles from the co-combustion of agricultural residues and sewage sludge may determine whether P is directly accessible for plant uptake or whether treatment by milling is required. The results here clearly show that the fuel admixing strategy is important, both for the types of phosphates that are formed (Falk et al., 2023) and also for the porosity and microstructure of the ash where the proximity of ash forming elements from admixed fuels determines the resulting compounds in the ash.

Further studies are needed to establish the size fraction of ash particles and their pore size distribution that are best suited to meet the needs of different plants, in addition to their water-holding capacity. The present work demonstrates the possibility of complementing XRT analysis with elemental and phase analyses from SEM-EDS and XRD, respectively, to identify and quantify volumes that have the potential to facilitate plant interaction. Such in-depth characterisation of ash fractions with higher resolution XRT and XRD to link phosphates to available surface areas after different milling strategies would be further work of interest. This should be accompanied with plant growth experiments where well-characterised ash fractions are milled to different particle sizes to evaluate their suitability for direct application.

4. Conclusions

The present work provided a unique 3D view of the volumetric share of phosphates, and their 3D distribution in slag particles from co-combustion of sewage sludge mixed with wheat straw or sunflower husks. This was achieved by combining X-ray micro-tomography (XRT) with XRD and SEM-EDS. Based on XRT data alone, neither the chemical nor phase composition can be determined, but a novel combination of these techniques enabled calculation of 3D phosphate distributions encompassing the entirety of the slag particle samples.

The phosphates are distinctly absent from iron- or silicate-rich regions, which highlights the tendency of phosphates to crystallise separate from the latter two even at high temperatures, in agreement with the literature. The predicted volumetric share of phosphates varied between 7 and 17 % for the sum of all phosphates in a single sample. The highest volumetric share of a single assigned phosphate was 17 %, observed in hard slag from WSS10 for $Ca_{9.5}Mg_{0.78}Fe_{0.22}(PO_4)_7$. The silicate-based slags derived from wheat straw and its admixtures generally display lower average X-ray attenuation compared to the more Ca-dominated sunflower husks mixtures. Higher resolution XRT may reveal if this is strictly due to chemical composition or if nano-porosity influences the measurements.

The average porosity varied between 15 and 35 vol% for the slag particles from the combustion of fuel mixtures containing sewage sludge, to 62 vol% for slag particles from the wheat straw combustion. For all samples, more than 60 % of the pores had an equivalent diameter below 30 μm, but pores with an equivalent diameter above 75 μm constituted the largest pore volume (75–92 vol%). Slag from sunflower husks mixtures have a slightly lower relative number of small pores and a greater pore volume consisting of pores over 75 μm compared to the slags from WS-containing fuels. The sphericity of pores in all samples

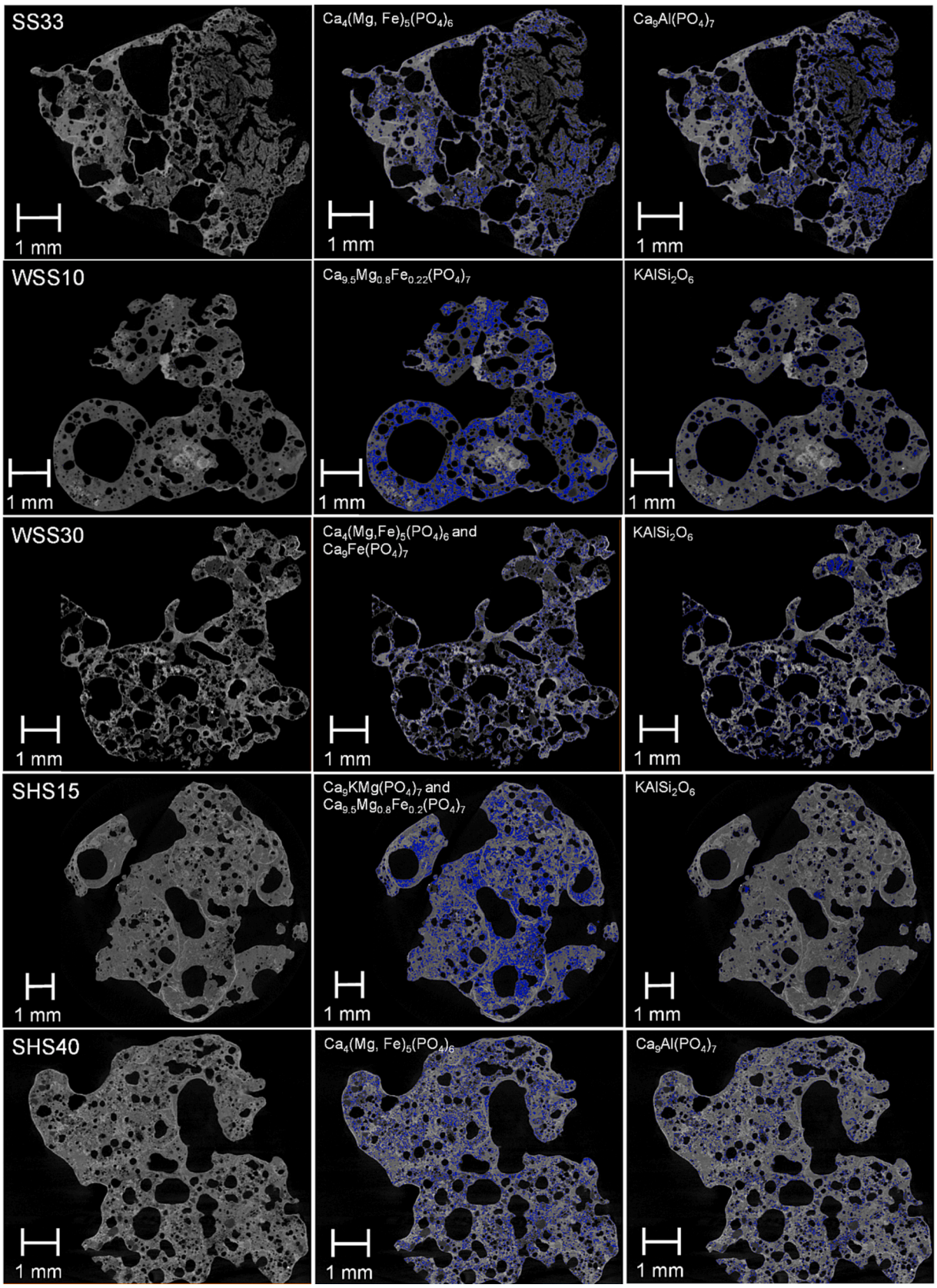

Fig. 4. Examples of cross-sections from XRT of hard slag particles. The middle and right columns show results from the image analysis that visualise the approximated distribution of P- and/or K-containing crystalline phases in blue. (For interpretation of the references to colour in this figure legend, the reader is referred to the web version of this article.)

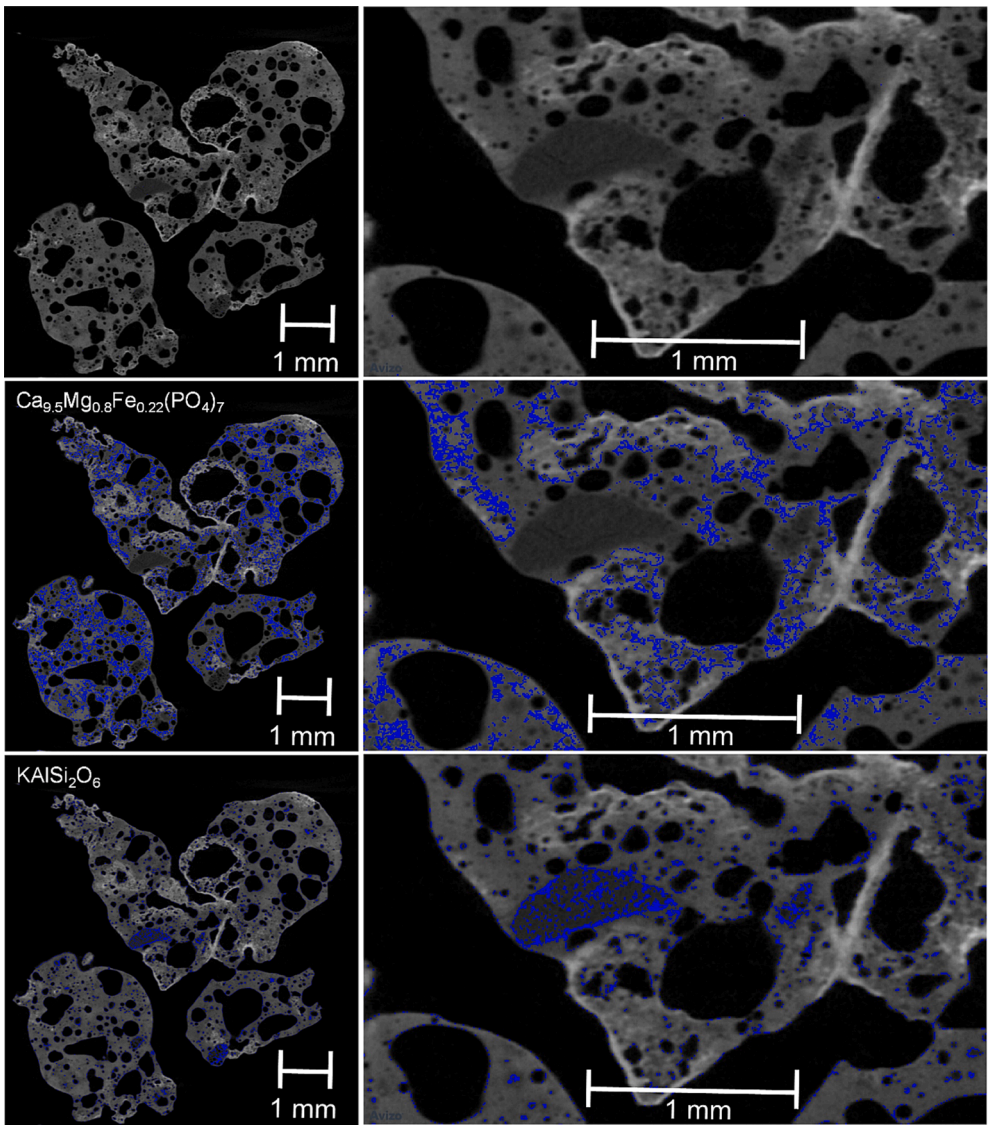

Fig. 5. Cross-section from XRT of WSS10 hard slag at the top left, followed underneath by results from the image analysis that visualise the approximated distribution of P- and K-containing crystalline phases, respectively, in blue. Zoomed-in views to the right. (For interpretation of the references to colour in this figure legend, the reader is referred to the web version of this article.)

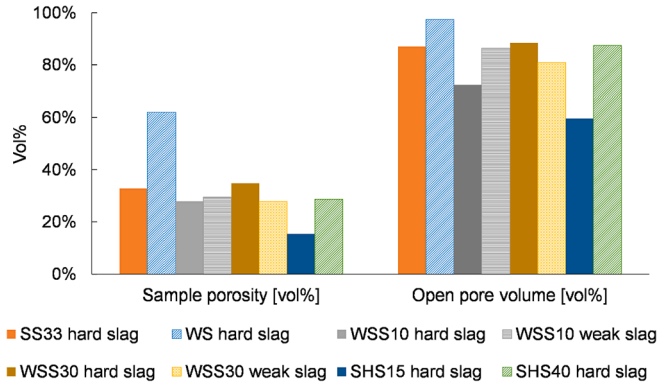

Fig. 6. Calculated average sample porosity and open pore volume.

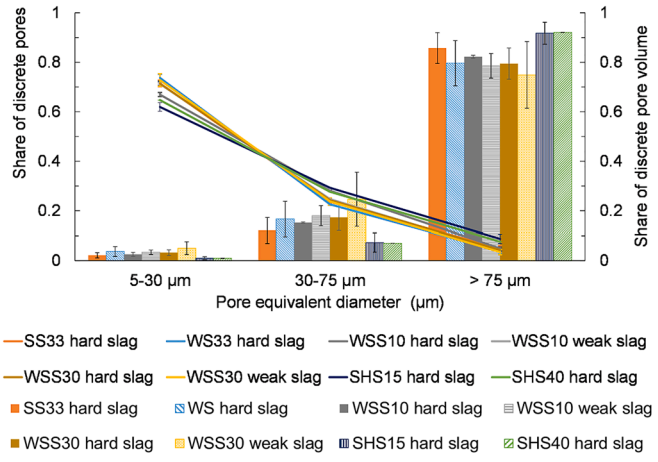

Fig. 7. Pore size distribution for the discrete pores, showing the relative number of pores with lines (left axis) and the relative pore volume with bars (right axis). Error bars represent one standard deviation.

decreases with their diameters.

CRediT authorship contribution statement

Anna Strandberg: Conceptualization, Methodology, Formal analysis, Investigation, Resources, Writing – original draft, Writing – review & editing, Visualization, Funding acquisition. **Mikael Thyrel:** Writing – review & editing, Supervision, Software, Project administration, Funding acquisition, Conceptualization. **Joel Falk:** Writing – review & editing, Investigation, Formal analysis. **Marcus Öhman:** Resources, Writing – review & editing, Funding acquisition. **Nils Skoglund:** Conceptualization, Methodology, Formal analysis, Investigation, Resources, Writing – review & editing, Funding acquisition.

Declaration of competing interest

The authors declare that they have no known competing financial interests or personal relationships that could have appeared to influence the work reported in this paper.

Data availability

Data will be made available on request.

Acknowledgements

We thank the foundation Carl-Fredrik von Horns fond and Stiftelsen för markvård till minne av Sanders Alburg, through the Royal Swedish Academy of Agriculture and Forestry Grant No. GFS2018-0099, the Swedish Research Council Grant No. 2017-05331, and Bio4Energy, a Strategic Research Environment supported through the Swedish Government's Strategic Research Area initiative, for supporting this work. Furthermore, financial support from the Swedish Research Council Formas is gratefully acknowledged under Grant No. 2018-00194 and Grant No. 2017-01613.

Dr. Johannes Koestel and Dr. Mats Larsbo at the X-ray facility of the Department of Soil and Environment, Swedish University of Agricultural Sciences, Sweden, is gratefully acknowledged for valuable assistance with the X-ray microtomography analysis. The facilities and technical support (Cheng Choo Lee) of the Umeå Core Facility for Electron Microscopy (UCEM) at the Chemical Biological Centre (KBC), Umeå University, National Microscopy Infrastructure, NMI (VR-RFI 2016-00968) is also greatly acknowledged. Dr. Eleonora Borén, M.Sc.Eng. Robert Lindgren, and M.Sc.Eng. Karin Sandström made valuable contributions during the combustion experimental campaign.

Appendix A. Supplementary data

Supplementary data to this article can be found online at https://doi.org/10.1016/j.wasman.2024.01.040.

References

Atienza–Martínez, M., Gea, G., Arauzo, J., Kersten, S.R.A., Kootstra, A.M.J., 2014. Phosphorus recovery from sewage sludge char ash. Biomass Bioenergy 65, 42–50. https://doi.org/10.1016/j.biombioe.2014.03.058.

Berger, M., Hubbell, J., Seltzer, S., Chang, J., Coursey, J., Sukumar, R., Zucker, D., Olsen, K., 2010. XCOM: Photon Cross Sections Database, NIST Standard Reference Database 8 (XGAM). Radiation Physics Division.

Cameron, K.C., Buchan, G.D., 2017. Porosity: Pore size distribution. Encyclopedia of Soil Science. CRC Press 1782–1785.

Cooper, J., Lombardi, R., Boardman, D., Carliell-Marquet, C., 2011. The future distribution and production of global phosphate rock reserves. Resour. Conserv. Recycl. 57, 78–86. https://doi.org/10.1016/j.resconrec.2011.09.009.

Edeh, I.G., Mašek, O., Buss, W., 2020. A meta-analysis on biochar's effects on soil water properties – New insights and future research challenges. Sci. Total Environ. 714, 136857 https://doi.org/10.1016/j.scitotenv.2020.136857.

Falk, J., Skoglund, N., Grimm, A., Öhman, M., 2020a. Fate of phosphorus in fixed bed combustion of biomass and sewage sludge. Energy Fuel 34, 4587–4594. https://doi.org/10.1021/acs.energyfuels.9b03976.

Falk, J., Skoglund, N., Grimm, A., Öhman, M., 2020b. Systematic evaluation of the fate of phosphorus in fluidized bed combustion of biomass and sewage sludge. Energy Fuel 34, 3984–3995. https://doi.org/10.1021/acs.energyfuels.9b03975.

Falk, J., Hannl, T.K., Ohman, M., Hedayati, A., Skoglund, N., 2023. Ash transformation during fixed-bed co-combustion of sewage sludge and agricultural residues with a focus on phosphorus. ACS Omega 8, 13162–13176. https://doi.org/10.1021/acsomega.3c00415.

Gorazda, K., Kowalski, Z., Wzorek, Z., 2012. From sewage sludge ash to calcium phosphate fertilizers. Pol. J. Chem. Technol. 14, 54–58.

Häggström, G., Hannl, T.K., Hedayati, A., Kuba, M., Skoglund, N., Öhman, M., 2021. Single pellet combustion of sewage sludge and agricultural residues with a focus on phosphorus. Energy Fuel 35, 10009–10022. https://doi.org/10.1021/acs.energyfuels.1c00882.

Hannl, T.K., Sefidari, H., Kuba, M., Skoglund, N., Öhman, M., 2020. Thermochemical equilibrium study of ash transformation during combustion and gasification of sewage sludge mixtures with agricultural residues with focus on the phosphorus speciation. Biomass Convers. Biorefin. 11, 57–68. https://doi.org/10.1007/s13399-020-00772-4.

Hedayati, A., Lindgren, R., Skoglund, N., Boman, C., Kienzl, N., Öhman, M., 2021. Ash transformation during single-pellet combustion of agricultural biomass with a focus on potassium and phosphorus. Energy Fuel. 35, 1449–1464. https://doi.org/10.1021/acs.energyfuels.0c03324.

Hedayati, A., Falk, J., Borén, E., Lindgren, R., Skoglund, N., Boman, C., Öhman, M., 2022. Ash transformation during fixed-bed combustion of agricultural biomass with a focus on potassium and phosphorus. Energy & Fuels. 36, 3640–3653. https://doi.org/10.1021/acs.energyfuels.1c04355.

Herzel, H., Krüger, O., Hermann, L., Adam, C., 2016. Sewage sludge ash — A promising secondary phosphorus source for fertilizer production. Sci. Total Environ. 542, 1136–1143. https://doi.org/10.1016/j.scitotenv.2015.08.059.

Herzel, H., Aydin, Z., Adam, C., 2021. Crystalline phase analysis and phosphorus availability after thermochemical treatment of sewage sludge ash with sodium and potassium sulfates for fertilizer production. J. Mater. Cycles Waste Manage. 23, 2242–2254. https://doi.org/10.1007/s10163-021-01288-3.

Kalasová, D., Dvořák, K., Slobodník, M., Všianský, D., Zikmund, T., Dluhoš, J., Váňa, R., Bureš, J., Kaiser, J., 2018. Characterization of inner structure of limestone by X-ray computed sub-micron tomography. Constr. Build. Mater. 174, 693–700. https://doi.org/10.1016/j.conbuildmat.2018.04.142.

Koestel, J., 2018. SoilJ: an ImageJ plugin for the semiautomatic processing of three-dimensional X-ray images of soils. Vadose Zone J. 17, 1–7.

Koestel, J., Larsbo, M., 2014. Imaging and quantification of preferential solute transport in soil macropores. Water Resour. Res. 50, 4357–4378.

Kratz, S., Vogel, C., Adam, C., 2019. Agronomic performance of P recycling fertilizers and methods to predict it: a review. Nutr. Cycl. Agroecosyst. 115, 1–39. https://doi.org/10.1007/s10705-019-10010-7.

Krüger, O., Adam, C., 2015. Recovery potential of German sewage sludge ash. Waste Manage. (oxford) 45, 400–406. https://doi.org/10.1016/j.wasman.2015.01.025.

Lidman Olsson, E.O., Glarborg, P., Dam-Johansen, K., Wu, H., 2023. Review of phosphorus chemistry in the thermal conversion of biomass: progress and perspectives. Energy Fuel 37, 6907–6998. https://doi.org/10.1021/acs.energyfuels.2c04048.

Ma, C., Skoglund, N., Carlborg, M., Broström, M., 2021. Structures and diffusion motions of K and Ca in biomass ash slags from molecular dynamics simulations. Fuel 302, 121072. https://doi.org/10.1016/j.fuel.2021.121072.

Mees, F., Swennen, R., Geet, M.V., Jacobs, P., 2003. Applications of X-ray computed tomography in the geosciences. Geol. Soc. Lond. Spec. Publ. 215, 1–6.

Moller, H.B., Jensen, H.S., Tobiasen, L., Hansen, M.N., 2007. Heavy metal and phosphorus content of fractions from manure treatment and incineration. Environ. Technol. 28, 1403–1418. https://doi.org/10.1080/09593332808618900.

Nordin, A., Strandberg, A., Elbashir, S., Åmand, L.-E., Skoglund, N., Pettersson, A., 2020. Co-combustion of municipal sewage sludge and biomass in a grate fired boiler for phosphorus recovery in bottom ash. Energies. 13, 1-28. ARTN 1708 10.3390/en13071708.

European Parliament and Council, 2023 Document 02019R1009-20230316 - Consolidated text: Regulation (EU) 2019/1009 of the European Parliament and of the Council of 5 June 2019 laying down rules on the making available on the market of EU fertilising products and amending Regulations (EC) No 1069/2009 and (EC) No 1107/2009 and repealing Regulation (EC) No 2003/2003. Official Journal of the European Union and available in EUR-Lex. http://data.europa.eu/eli/reg/2019/1009/2023-03-16.

Pettersson, A., Åmand, L.-E., Steenari, B.-M., 2008. Leaching of ashes from co-combustion of sewage sludge and wood—Part I: Recovery of phosphorus. Biomass Bioenergy 32, 224–235.

Rasa, K., Heikkinen, J., Hannula, M., Arstila, K., Kulju, S., Hyväluoma, J., 2018. How and why does willow biochar increase a clay soil water retention capacity? Biomass Bioenergy 119, 346–353. https://doi.org/10.1016/j.biombioe.2018.10.004.

Reinmöller, M., Schreiner, M., Guhl, S., Neuroth, M., Meyer, B., 2019. Ash behavior of various fuels: The role of the intrinsic distribution of ash species. Fuel 253, 930–940. https://doi.org/10.1016/j.fuel.2019.05.036.

Richardson, K., Steffen, W., Lucht, W., Bendtsen, J., Cornell, S.E., Donges, J.F., Drüke, M., Fetzer, I., Bala, G., von Bloh, W., Feulner, G., Fiedler, S., Gerten, D., Gleeson, T., Hofmann, M., Huiskamp, W., Kummu, M., Mohan, C., Nogués-Bravo, D., Petri, S., Porkka, M., Rahmstorf, S., Schaphoff, S., Thonicke, K., Tobian, A., Virkki, V., Wang-Erlandsson, L., Weber, L., Rockström, J., 2023. Earth beyond six of nine planetary boundaries. Sci. Adv. 9, 16. https://doi.org/10.1126/sciadv.adh2458.

Rockström, J., Steffen, W., Noone, K., Persson, Å., Chapin, F.S., Lambin, E., Lenton, T.M., Scheffer, M., Folke, C., Schellnhuber, H.J., Nykvist, B., de Wit, C.A., Hughes, T., van der Leeuw, S., Rodhe, H., Sörlin, S., Snyder, P.K., Costanza, R., Svedin, U., Falkenmark, M., Karlberg, L., Corell, R.W., Fabry, V.J., Hansen, J., Walker, B., Liverman, D., Richardson, K., Crutzen, P., Foley, J., 2009. Planetary boundaries, exploring the safe operating space for humanity. Ecol. Soc. 14.

Schindelin, J., Arganda-Carreras, I., Frise, E., Kaynig, V., Longair, M., Pietzsch, T., Preibisch, S., Rueden, C., Saalfeld, S., Schmid, B., 2012. Fiji: an open-source platform for biological-image analysis. Nat. Methods 9, 676.

Schneider, C.A., Rasband, W.S., Eliceiri, K.W., 2012. NIH Image to ImageJ: 25 years of image analysis. Nat. Methods 9, 671.

Schoumans, O.F., Bouraoui, F., Kabbe, C., Oenema, O., van Dijk, K.C., 2015. Phosphorus management in Europe in a changing world. Ambio 44, 180–192. https://doi.org/10.1007/s13280-014-0613-9.

Skoglund, N., Grimm, A., Öhman, M., Boström, D., 2014. Combustion of biosolids in a bubbling fluidized bed, part 1: main ash-forming elements and ash distribution with a focus on phosphorus. Energy Fuel 28, 1183–1190. https://doi.org/10.1021/ef402320q.

Steffen, W., Richardson, K., Rockström, J., Cornell, S.E., Fetzer, I., Bennett, E.M., Biggs, R., Carpenter, S.R., de Vries, W., de Wit, C.A., Folke, C., Gerten, D., Heinke, J., Mace, G.M., Persson, L.M., Ramanathan, V., Reyers, B., Sörlin, S., 2015. Planetary boundaries: Guiding human development on a changing planet. Science 347. https://doi.org/10.1126/science.1259855.

Strandberg, A., Thyrel, M., Skoglund, N., Lestander, T.A., Broström, M., Backman, R., 2018. Biomass pellet combustion: Cavities and ash formation characterized by synchrotron X-ray micro-tomography. Fuel Process. Technol. 176, 211–220. https://doi.org/10.1016/j.fuproc.2018.03.023.

Strandberg, A., Skoglund, N., Thyrel, M., 2021. Morphological characterisation of ash particles from co-combustion of sewage sludge and wheat straw with X-ray microtomography. Waste Manag. 135, 30–39. https://doi.org/10.1016/j.wasman.2021.08.019.

Van de Velden, M., Dewil, R., Baeyens, J., Josson, L., Lanssens, P., 2008. The distribution of heavy metals during fluidized bed combustion of sludge (FBSC). Journal of Hazardous Materials. 151, 96–102. https://doi.org/10.1016/j.jhazmat.2007.05.056.

Van Dijk, K.C., Lesschen, J.P., Oenema, O., 2016. Phosphorus flows and balances of the European Union Member States. Sci. Total Environ. 542, 1078–1093. https://doi.org/10.1016/j.scitotenv.2015.08.048.

Zhao, Y., Ren, Q., Na, Y., 2018. Phosphorus transformation from municipal sewage sludge incineration with biomass: formation of apatite phosphorus with high bioavailability. Energy Fuel 32, 10951–10955. https://doi.org/10.1021/acs.energyfuels.8b01915.

Zhu, F., Cakmak, E.K., Cetecioglu, Z., 2023. Phosphorus recovery for circular economy: Application potential of feasible resources and engineering processes in Europe. Chem. Eng. J. 454, 140153.